

Seismic waveform-coherence controlled by earthquake source dimensions

Tong Zhou^{1,2}, Lingsen Meng¹, Ailin Zhang³ and Jean-Paul Ampuero⁴

¹Earth, Planetary and Space Sciences, University of California, Los Angeles, Los Angeles, 90095, USA

²now at Aramco Research Center - Beijing, Aramco Asia, Beijing, 100102, China

³University of Michigan-Shanghai Jiao Tong University Joint Institute, Shanghai Jiao Tong University, Shanghai, 200240, China

⁴Université Côte d'Azur, IRD, CNRS, Observatoire de la Côte d'Azur, Géoazur, Valbonne, 06560, France

Key Points:

- Waveform coherence decays as a function of inter-station distance faster for large earthquakes ($M_w > 7$).
- The waveform coherence pattern is governed by earthquake source size.
- Rupture sizes inferred from waveform coherence satisfy empirical scaling relations.

Corresponding author: Lingsen Meng, meng@epss.ucla.edu

Corresponding author: Tong Zhou, tzhou@epss.ucla.edu

This is the author manuscript accepted for publication and has undergone full peer review but has not been through the copyediting, typesetting, pagination and proofreading process, which may lead to differences between this version and the [Version of Record](#). Please cite this article as [doi: 10.1029/2021JB023458](https://doi.org/10.1029/2021JB023458).

This article is protected by copyright. All rights reserved.

Abstract

Rupture size is a fundamental earthquake source parameter that is challenging to infer independently from far-field seismological observations. Here we develop a novel observational constraint on source size based on the decay rate of wavefield coherence across a seismic array. For a given earthquake, waveform coherence decays with increasing inter-station distance or, more precisely, with increasing projection difference defined as the difference between the take-off vectors associated to the two stations projected along the rupture direction. We find that coherence generally falls off with projection difference faster for earthquakes of larger magnitudes. The magnitude dependence of the coherence decay rate can be explained by a finite source effect: larger source sizes cause larger differences of phase delays between waves arriving from different parts of the rupture at different stations, hence a stronger spatial variability of the wavefield, resulting in a breakdown of waveform coherence. Assuming a 1D Haskell's source model, the rupture size can be estimated from the coherence decay rate. We apply this method to USArray data of earthquakes in three subduction zones, the Sea of Okhotsk, South America and Japan. The source sizes inferred from the coherence decay patterns are consistent with scaling relations intermediate between width-saturated L-models and quasi-equi-dimensional rupture models. Our observation captures a unique pattern of array waveform coherence and demonstrates the potential of utilizing waveform coherence to study earthquake source parameters.

Plain Language Summary

In this paper, we observe that for a given earthquake, the similarity of waveform (coherence) recorded by stations in a far-field array decays with increasing inter-station distance. The waveform coherence generally falls off with inter-station distance faster for earthquakes of larger magnitudes and therefore, larger rupture sizes. We develop a novel method using array waveform coherence to estimate the earthquake rupture size, and apply this method to USArray data of earthquakes in three geological regions: the Sea of Okhotsk, South America and Japan. The source sizes inferred from the coherence decay patterns are consistent with previous studies using different methods. According to our observation, there is a potential to infer earthquake rupture independently from far-field observations by waveform coherence.

1 Introduction

Over the last two decades, the development of large-aperture seismic arrays, such as USArray, the European seismic networks and Hi-net network, has enabled a broad spectrum of seismological studies. The dense spatial sampling of arrays has enabled significant progress in the study of Earth's interior and earthquake source, such as constraining 3D mantle structures beneath North America (e.g., Shen & Ritzwoller (2016); Burdick et al. (2017)), detecting deep earth discontinuities (e.g. Lin et al. (2013); Poli et al. (2015)), imaging the rupture processes of large earthquakes using back-projection methods (e.g. Kiser & Ishii (2017); Meng et al. (2018)), and improving earthquake detection capabilities using template matching techniques (Gibbons & Ringdal, 2006; Peng & Zhao, 2009). Coherence-based detection methods are also applied to detect non-volcanic tremors (e.g. Shelly et al. (2007); Obara (2012)), anthropogenic signals (Riahi & Gerstoft, 2015), closely located earthquakes or tremors with non-matching waveforms (Hawthorne & Ampuero, 2018), and source kinematics by stereometry (Mordret et al., 2020).

While array waveform coherence has been widely applied to earthquake detection, here we exploit it to constrain earthquake source parameters, in particular rupture dimensions. Current methods to study source parameters are mostly based on deterministic waveform fitting. Finite source inversion applied to teleseismic recordings to resolve slip distributions (Ji et al., 2002) constrain rupture duration T and moment, but suffer from a strong tradeoff between source size L and rupture speed V_r ($T = L/V_r$). Hawthorne et al. (2019) introduced an approach to estimate the rupture size of low frequency earthquakes from the inter-station fluctuations of inter-event normalized cross-spectra, a waveform coherence property controlled by differences between the apparent source time functions viewed by each station.

Here we examine the relationship between earthquake rupture dimension and array waveform coherence, i.e., the normalized cross-correlation coefficient between waveforms recorded by pairs of stations within an array. The idea of exploring array waveform coherence is originally motivated by applications of seismic array processing to imaging Earth's structure and earthquake sources. The coherence length of an array, defined as the maximum inter-station distance with adequate waveform coherence, is a key constraint on array design that determines the maximum array aperture to apply a back-projection analysis to image sources or structures. Previous work indicates that wave-

77 form coherence decays dramatically with increasing inter-station distance and frequency
78 (e.g. Zerva & Zervas (2002); Langston (2014)). In these studies based on local seismic
79 phases, waveform incoherence mostly results from wave scattering by crustal heterogeneities.
80 In contrast, teleseismic waveforms involve rather simple path effects, and thus provide
81 a unique opportunity to study the effects of earthquake source properties on waveform
82 coherence and to assess the potential of using array waveform coherence to constrain earth-
83 quake rupture sizes.

84 By analyzing the coherence patterns of a variety of teleseismic earthquakes recorded
85 by the USArray, we observe that the waveform coherence decays faster with increasing
86 inter-station distance and earthquake magnitude. This magnitude dependence of the co-
87 herence decay rate can be explained by a finite source effect. From the representation
88 theorem, the far-field body wave seismograms of a finite-fault rupture are the integral
89 of slip rate functions distributed along the fault surface convolved with the Greens func-
90 tion of each fault point (Aki & Richards, 2002). The arrival times at an array of waves
91 coming from different parts of a rupture depend on the rupture front propagation (rup-
92 ture times) and on wave propagation (travel times of the Greens functions). The latter
93 depend both on source and receiver locations. Therefore, increasing either the source size
94 or inter-station distance can cause a larger delay between waves from different parts of
95 the source, resulting in a breakdown of waveform coherence.

96 The decay rate of waveform coherence is observed to satisfy a relatively simple re-
97 lation under the assumption of 1D Haskell's source model, which has the potential to
98 be used for estimating the rupture sizes of earthquakes with saturated seismogenic width.
99 Moreover, it is remarkable that the waveform coherence decay rate does not depend on
100 rupture velocity V_r , which naturally circumvents the trade-off between rupture length
101 L and rupture velocity V_r (Ide, 2007) in methods based on teleseismic finite-fault inver-
102 sion. Nevertheless, there are still questions to be solved before applying this method to
103 general earthquakes. First, it is difficult yet significant to separate the source-induced
104 and path/station-induced incoherent components so that the teleseismic waveform co-
105 herence will only focus on the source parameters. Second, other complex source param-
106 eters influence the teleseismic waveform coherence decay. For example, the unsaturated
107 seismogenic width W (quasi-equal-dimensional rupture), the bilateral rupture, and the
108 aspect ratio L/W .

109 In this paper, we investigate the finite-source controlled waveform coherence de-
 110 cay in detail. First, we demonstrate the teleseismic waveform coherence pattern predicted
 111 by a 1D Haskell’s source model and find a relation between inter-station waveform co-
 112 herence and projection difference, a measurement of inter-station difference between take-
 113 off vectors projected along the rupture direction. The inter-station coherence falls off as
 114 a function of projection difference and earthquake rupture length. Second, we study the
 115 inter-station coherence of teleseismic earthquake waveforms recorded by USArray in East-
 116 ern US. For a given earthquake, we find that inter-station coherence decays as a func-
 117 tion of projection difference and magnitude (related to the rupture size). Next, we es-
 118 timate the rupture lengths by fitting the coherence decay rate and projection difference,
 119 and assess the uncertainty of the estimated rupture length. We investigate the moment-
 120 size scaling relationship between the coherence estimated rupture dimensions and mo-
 121 ment magnitudes. Finally, we address the impacts of source complexities on the rupture
 122 size estimation, including finite-frequency, aspect ratio, and bilateral rupture.

123 2 Elongated Haskell’s Source Model

124 To demonstrate the hypothesis that source size controls the decay pattern of inter-
 125 station coherence, we establish an analytical relationship between inter-station coher-
 126 ence and the source size of a unilateral rupture. Following Haskell (1964), we assume an
 127 elongated rectangular rupture with uniform slip, length L and width W such that $L \gg$
 128 W , embedded in a 3D homogeneous elastic space, propagating unilaterally at constant
 129 rupture speed V_r along the L direction, with a uniform invariant trapezoidal slip-rate func-
 130 tion (Figure 1). This simple setting is intended to isolate the effect of source size on wave-
 131 form coherence. An array is located at the teleseismic distance R_0 . For a seismic ray go-
 132 ing from the hypocenter to a station, we denote the azimuth relative to the rupture prop-
 133 agation vector as ϕ and the take-off angle as θ . We define the take-off projection γ as
 134 the projection of the take-off vector onto the rupture direction ($\gamma = \sin \theta \cos \phi$, red ar-
 135 row in Figure 1).

136 The far-field displacement u at a receiver at distance r and take-off projection γ ,
 137 relative to the hypocenter, is the integral of the contributions from all points (at distance
 138 x from the hypocenter) along the rupture:

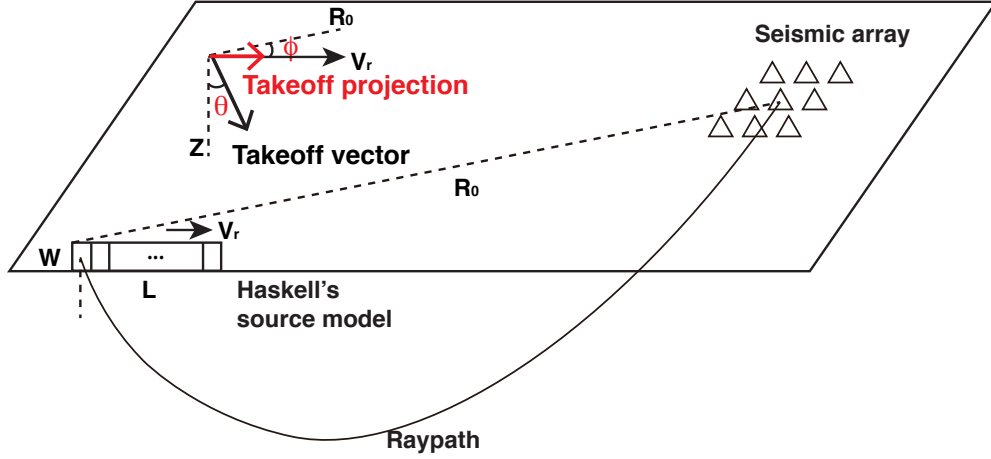


Figure 1. Conceptual description of a Haskell's source model recorded by a teleseismic array and definition of the take-off projection.

$$u(r, \gamma, t) = \frac{\mu W}{4\pi\rho c^3} \int_0^L \frac{R}{r} \dot{D}\left(t - \frac{r}{c} - \frac{x}{V_r} + \frac{\gamma x}{c}\right) dx, \quad (1)$$

where c is the P wave speed, t the time, μ the rigidity, ρ the density, R the radiation pattern, and \dot{D} the slip rate function. Equation (1) accounts for an integration along the rupture length L , which is assumed much smaller than the source-receiver distance.

Taking the Fourier transform, we get

$$U(r, \gamma, \omega) = \frac{\mu RW}{4\pi\rho c^3 r} \dot{D}(\omega) e^{-\frac{i\omega r}{c}} \int_0^L e^{-i\omega\left(\frac{x}{V_r} - \frac{\gamma x}{c}\right)} dx. \quad (2)$$

Integrating equation (2) along the whole rupture length L , we get

$$U(r, S, \omega) = \frac{\mu RW}{4\pi\rho c^3 r} \dot{D}(\omega) e^{-\frac{i\omega r}{c}} \frac{1}{\omega S} \sin\left(\frac{\omega L}{2} S\right) e^{-\frac{i\omega L}{2} S}, \quad (3)$$

where S is a slowness term:

$$S = \frac{1}{V_r} - \frac{\gamma}{c}. \quad (4)$$

Equation (3) does not consider receiver-side scatterings and site effects. Convolution with a term representing these effects $G e^{-i\omega g}$, we get

$$U = \frac{\mu RWG}{4\pi\rho c^3 r} \dot{D}(\omega) \frac{1}{\omega S} \sin\left(\frac{\omega L}{2} S\right) \exp\left[-i\omega\left(\frac{r}{c} + \frac{LS}{2} + g\right)\right]. \quad (5)$$

The coherence spectrum between the seismograms recorded at stations A and B, defined from the normalized cross-spectrum at frequency ω , can be written as:

$$CC(\omega) = \frac{\text{Real}(U(S_A, \omega) \cdot U^*(S_B, \omega))}{|U(S_A, \omega)| \cdot |U(S_B, \omega)|} = \cos\left[-\frac{\omega L}{2c}(\gamma_A - \gamma_B) + \omega(g_A - g_B)\right]. \quad (6)$$

The detailed derivation of Equation (6) is given in the appendix. We define the projection difference as the difference of take-off projections between two stations, $d_p = \gamma_A - \gamma_B$ (Figure 1). The projection difference is related to both the inter-station distance and the take-off angle. We also define the error difference as $\delta = \omega(g_A - g_B)$, which accounts for the difference of local scatterings and site effects between the two stations. Equation (6) shows that inter-station coherence is affected by three factors: the source rupture size L , the inter-station projection difference (related to the inter-station distance), and frequency. In particular, a larger rupture length L or increase in frequency results in a smaller coherence; therefore, faster coherence decay as a function of projection difference is expected for larger earthquakes in the same passband.

3 Waveform coherence decay measurements

Besides the 1D unilateral Haskell's rupture model, we seek to find seismic waveform coherence decay controlled by earthquake size in real teleseismic array data. Here we select teleseismic earthquake events (located at distances between 30° and 90° from the array center) with moment magnitude $M_w > 6.2$ recorded by the USArray in eastern US (Figure 2). The crustal structures beneath Eastern US are relatively simple compared with the locations of other large regional arrays, e.g., western US and Europe. Therefore, their inter-station coherence patterns are less affected by crustal scattering at the array side. The teleseismic P wave has a nearly vertical incident angle, therefore we only consider vertical-component seismograms with signal-to-noise ratio (SNR) above 2.5. The SNR is defined here as the ratio of the root mean square amplitude of the signal and noise, measured in 10-s-long windows starting at the P arrival and at 20 s before P arrival, respectively. The array recordings are band-pass filtered in three frequency bands: 0.25-0.5, 0.5-1 and 1-2 Hz. We align the filtered waveforms by cross-correlating their initial

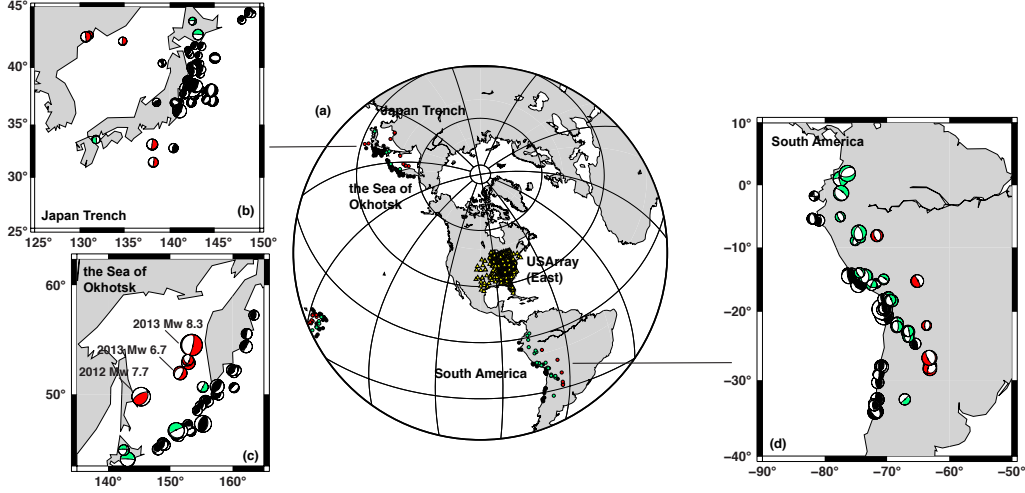


Figure 2. Array and earthquakes used in this study for waveform coherence measurement. (a) global view of earthquakes and seismic array (USArray in the Eastern United States, operating from 2011 to 2015); Selected events in (b) Japan, (c) the Sea of Okhotsk, and (d) South America subduction zone. Focal mechanisms (beachballs) and dots are color coded by depth: >300 km in red, 70-300 km in green, and <70 km in black.

173 P arrivals at each frequency band with a window length of 15, 8 and 6 seconds, respec-
 174 tively, in order to mitigate the travel time errors due to unmodeled velocity structure.
 175 To ensure the robustness of the coherence measurements, we only select events with more
 176 than 100 aligned waveform traces. In total, 192 events are incorporated into the anal-
 177 ysis, where 127 of them are shallow earthquakes (< 70 km), 35 of them are intermediate-
 178 depth earthquakes (70 – 300 km) and 30 of them are deep-focus earthquakes (> 300
 179 km). The number of stations for each selected earthquake varies a little but does not af-
 180 fect the aperture of the array too much. The studied earthquakes cover three major sub-
 181 duction zones: the Sea of Okhotsk, Japan, and South America (Figure 2).

182 We computed waveform coherence, in each frequency band, using the normalized
 183 cross-correlation coefficient (CC) between all the station pairs defined as

$$CC = \frac{\int_{t_s}^{t_e} u_1(x_1, t) \cdot u_2(x_2, t) dt}{\int_{t_s}^{t_e} |u_1(x_1, t)|^2 dt \int_{t_s}^{t_e} |u_2(x_2, t)|^2 dt}, \quad (7)$$

184 where u_1 and u_2 are the filtered waveforms of two different stations in the time win-
 185 dow $[t_s, t_e]$. x_1 and x_2 denote the location of each station related to the hypocenter. The

186 selected time windows start at the initial P arrival and have a duration equal to the source
187 duration according to the global centroid moment tensor (gCMT) catalog (Ekström et
188 al., 2012). Such windows are sufficiently long to record the whole rupture process but
189 short enough to avoid coda waves with low coherence. Each event has on average ap-
190 proximately 20,000 unique station pairs. To statistically quantify the coherence pattern,
191 we group station pairs into bins of inter-station distances, with an interval of 50 km, and
192 investigate the median coherence of each bin as a function of inter-station distance. For
193 each distance bin, we also report the standard deviation of the median coherence obtained
194 by bootstrapping based on 100 realizations of 85% randomly selected station combina-
195 tions (Efron & Tibshirani, 1994).

196 To demonstrate the array coherence patterns, we select three deep earthquakes with
197 depths ranging from 591 to 632 km beneath the Sea of Okhotsk (Figure 2c). The Mw
198 8.3 Okhotsk earthquake C201305240544A (gCMT event ID) is the largest deep-focus earth-
199 quake ever recorded and has been well-documented in previous studies including finite
200 source inversions, multiple source inversions, back-projection and directivity analysis (Wei
201 et al., 2013; Ye et al., 2013; Chen et al., 2014; Meng et al., 2014; Zhan et al., 2014; Park
202 & Ishii, 2015). The Mw 6.7 event B20130524145A occurred near the source region of the
203 Mw 8.3 event, and the Mw 7.7 earthquake C201208140259A occurred in the southern
204 region of the sea of Okhotsk subduction zone. The duration of the Mw 8.3, 7.7 and 6.7
205 events, which we set as window duration to measure waveform coherence, are 71, 35 and
206 11 seconds, respectively, according to global centroid moment tensor solutions (Ekström
207 et al., 2012). Considering the large epicentral distance to the array (about 60°), the record-
208 ings of these events share similar path effects; therefore, coherence differences among them
209 are mainly controlled by source effects.

210 The Mw 6.7 earthquake has smaller source effects than the other two earthquakes.
211 The coherence for this event (Figure 3a) is above 0.9 in the 0.25-0.5 and 0.5-1 Hz fre-
212 quency bands. Remarkably, coherence remains high up to inter-station distances exceed-
213 ing 1000 km. The slow coherence decay with inter-station distance suggests that the source
214 effect of this earthquake is small. The baseline coherence in the frequency bands of 0.25-
215 0.5, 0.5-1 and 1-2 Hz is 0.96, 0.92, and 0.78, respectively. The lower coherence at higher
216 frequency is expected due to wave scattering in the 3D velocity structure.

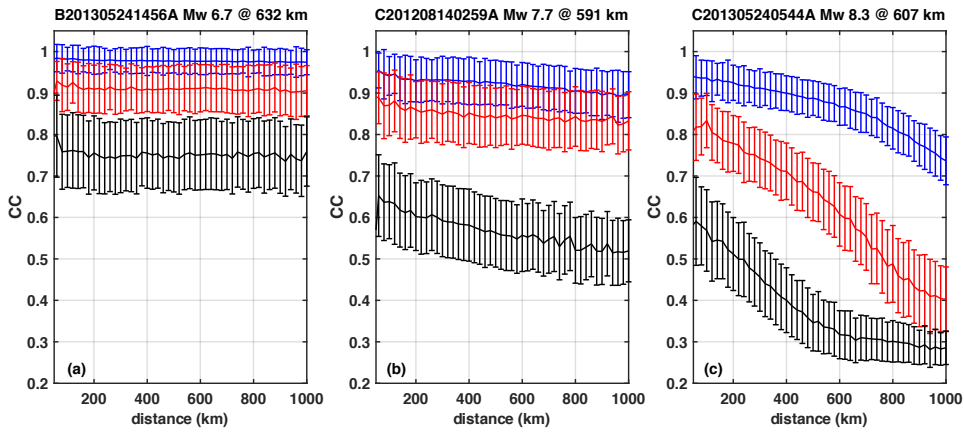


Figure 3. Waveform coherence (CC) as a function of inter-station distance for three deep earthquakes beneath the Sea of Okhotsk recorded by the USArray in Eastern US in 3 frequency bands: 0.25-0.5 Hz (blue), 0.5-1 Hz (red) and 1-2 Hz (black).

As the magnitudes (and therefore earthquake rupture sizes) increase, we observe a significant coherence decay as a function of both inter-station distance and frequency. In the 0.25-0.5 and 0.5-1 Hz frequency bands, the coherence of the Mw 7.7 earthquake decays about 0.05 over a distance range of 1000 km. The Mw 8.3 event shows even faster inter-station coherence decay, from 0.95 to 0.8 and from 0.8 to 0.4, respectively. In the 1-2 Hz band, the coherence of the Mw 7.7 and Mw 8.3 events decays with inter-station distance from 0.65 to 0.5 and from 0.6 to 0.3, respectively.

In principle, the CC value should be 1 at zero inter-station distance. However, we measure CC values smaller than 1 at zero distance, especially at higher frequencies (Figure 3). There are two potential explanations: (1) the minimum station interval of the US array is around 30 km, therefore our CC values at distance zero are extrapolation and may not capture a possible steeper coherence decay within the first 30 km. (2) The inter-station waveform coherence is also affected by the velocity structure right beneath the station site, and spatial variability of site effects can significantly lower the coherence (e.g., one station might be on a rock site and the other is on a nearby sedimentary basin). Such local scattering difference can be described by the 'error difference' term in equation (6). We also observe in Figure 3 that the CC value at the minimum inter-station distance decays with increasing frequency, consistent with the expectation that

235 higher frequency waveforms are more affected by local scatterings and site effects. Given
 236 such observation, we choose for our further analysis of source effect the two lower fre-
 237 quency bands, 0.25-0.5 and 0.5-1 Hz. Both frequency bands satisfy the condition that
 238 $CC > 0.7$ at the minimum inter-station distance for the Mw 8.3 earthquake. There-
 239 fore, they are the highest frequency bands where the scattering due to velocity hetero-
 240 geneities does not strongly affect the coherence pattern.

241 4 Constraining Earthquake Dimensions with Coherence Decay Rates

242 4.1 Earthquake size estimation based on 1D unilateral Haskell's source 243 model

244 From equation (6), a linear relationship between the arc cosine of CC and the pro-
 245 jection difference can be derived:

$$\text{acos}(CC) = \frac{\omega L d_p}{2c} + \delta. \quad (8)$$

246 Equation (8) shows that $\text{acos}(CC)$ scales with projection difference via a factor of
 247 $\omega L/2c$. The error difference, δ , is assumed independent on projection difference d_p be-
 248 cause the site effects only depend on shallow velocity structures beneath each station,
 249 which we treat as stochastic in space. This means δ is non-zero, which leads to $\text{acos}(CC) <$
 250 1 at $d_p = 0$. This again explains why the actual CC measurement is always smaller than
 251 1 at zero inter-station distance.

252 We perform a linear fitting using equation (8) to find the best $\omega L/2c$ (slope) and
 253 δ (intercept) for each earthquake. Figure 4a-f shows the fitting result of the three deep
 254 earthquakes beneath the Sea of Okhotsk in the 0.25-0.5 and 0.5-1 Hz frequency bands.
 255 Here we focus on the slope and estimate the rupture length L . The uncertainty of the
 256 fitted slope is derived from the uncertainty of CC measurements (see section 2.1) using
 257 an error propagation theorem (Bevington & Robinson, 2002).

258 In the two frequency ranges, the data from all three earthquakes satisfy the linear
 259 relationship between $\text{acos}(CC)$ and projection difference d_p in equation (8) (Figure 4a-
 260 f). Theoretically, the estimated rupture length should be independent of the measure-
 261 ment frequency band. This is verified for the Mw 8.3 earthquake (Figure 4b and e). How-
 262 ever, for the Mw 6.7 earthquake, the relatively flat $\text{acos}(CC)$ curve suggests that the fi-

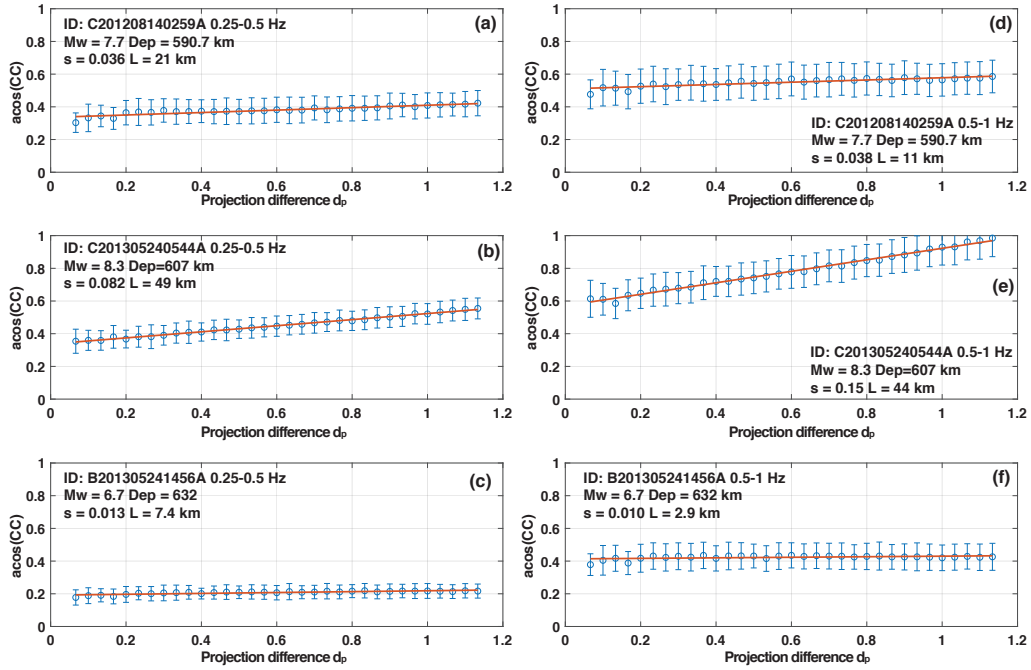


Figure 4. Coherence decay curve as a function of projection difference d_p and the inferred rupture length for the three selected deep earthquakes under the Sea of Okhotsk. Events are labeled with gCMT ID. Two frequency bands are considered: 0.25-0.5 Hz (left columns) and 0.5-1 Hz (right columns). Blue: observations; red: best-fitting lines. In each panel, the slope of the relation between $\text{acos}(\text{CC})$ and d_p is indicated as s and the estimated rupture length as L .

263 nite source effect is small, and the source size is difficult to be constrained from the co-
264 herence pattern. For small earthquakes, the observed inter-station coherence fluctuation
265 is not controlled by finite-source effects, but rather by path effects and array-side scat-
266 tering, which makes the estimation of rupture length from array coherence decay rate
267 less robust for small earthquakes. The Mw 7.7 earthquake also shows a discrepancy of
268 the estimated rupture length in two frequency bands. In fact, a complex rupture pro-
269 cess including bilateral rupture and low aspect ratio (L/W) can also influence the esti-
270 mation of rupture length and bring uncertainties. Therefore, the simple model is only
271 suitable for earthquakes with elongated rupture ($L/W \gg 1$). We listed all the linear
272 fitting results for M7+ earthquakes in the supplementary material.

273 We notice that the estimated rupture length L is underestimated. For example, the
274 coherence-based rupture length estimation for the Mw 8.3 earthquake in the Sea of Okhotsk
275 is about 49 km. However, teleseismic back-projection gives a rupture size of around 145
276 km, comprising a 40-km-long northward propagating segment and a 110-km-long south-
277 ward propagations (Meng et al., 2014). Finite fault inversion results show even larger
278 rupture length around 195-220 km (Ye et al., 2013; Wei et al., 2013). The interference
279 effect of bilateral rupture fronts underestimates the rupture length by 1/2 (see section
280 5.2), resulting a calibrated rupture length estimation of 98 km. The remaining under-
281 estimation is possibly caused by the gap between Haskell’s rupture model and source com-
282 plexities, including the aspect ratio (L/W), heterogeneous slip distribution, etc. (see sec-
283 tion 5.2).

284 4.2 The Moment-Size Scaling Relations

285 Real earthquakes are far from 1D Haskell’s model, which leads to systematic er-
286 ror of the coherence-measured rupture length. However, the coherence method is still
287 useful because it can capture the order-of-magnitude of the earthquake rupture size, and
288 distinguish different moment-size scaling relations. Here we analyze the scaling relation
289 between earthquake rupture size inferred from array coherence decay and the moment
290 magnitude. The seismic moment is defined as: $M_0 = \mu DA$, where μ is the shear mod-
291 ulus, D the average slip and A the rupture area. Since both D and A depend on rup-
292 ture size, the moment can be regarded as proportional to a power of rupture size, i.e.,
293 $M \propto L^n$. Considering the definition of moment magnitude $M_w = (\log M - 9.1)/1.5$,
294 we have

$$\log L \propto \frac{3}{2n} M_w, \quad (9)$$

Therefore, the logarithm of rupture size has a linear relation with moment magnitude and the slope (k-value, $k = 3/2n$) represents the power-law factor of the scaling relation.

We analyze the scaling relation between the coherence-decay estimated $\log L$ and moment magnitude in the three study regions: the sea of Okhotsk, Japan and South America subduction zones (Figure 5). Compared to the measurements showing large error bars in the frequency band of 0.5-1 Hz (Figure 5(g-1)), the source size measurements performed in the frequency band of 0.25-0.5 Hz yields more stable estimations (Figure 5(a-f)), which is possibly because of even smaller scatterings and path effects. Therefore, we mainly analyze the scaling relations estimated with the frequency band of 0.25-0.5 Hz.

To analyze the effects of moment magnitude ranges on k-value, we fit the linear scaling relation between $\log L$ and M_w in two magnitude ranges: M6.2+ and M7+. The uncertainties of the rupture size estimation of M7+ earthquakes (the error bars in Figure 5b,d and f) are generally smaller than M6 class earthquakes (the error bars in Figure 5a,c and e). Thus, we consider that the k-value estimation is more stable for M7+ earthquakes. The coherence-decay estimated rupture size of M6 class earthquakes yields larger uncertainty and scattering because of two factors. First, although the minimum measuring frequency 0.25 Hz is generally above the theoretical first corner frequency of M6+ earthquakes (around 0.1 Hz, Geller (1976)), which enables the observation of finite source effects, the variation of corner frequencies (e.g., in the Japan region, 0.25 Hz, Izutani & Kanamori (2001)) may lead to less observable finite source effects. Second, as discussed earlier, M6 class earthquakes have smaller array coherence decay rate from finite source effects, thus the array coherence decay measurements are more likely to be affected by scatterings and local heterogeneities along the path and at the station side.

We then compare the coherence-inferred k-value with previous studies. Theoretically, k-value depends on the magnitude range of earthquakes. For large earthquakes (M 7+), the rupture width W saturates and two end-member models are possible: the L-model with $D \propto L$, implying $n=2$ and $k=0.75$, and the W-model with $D \propto W$, implying $n=1$ and $k=1.5$ (Romanowicz & Rundle, 1993). For smaller earthquakes (M 6) which have quasi-equal rupture dimensions, $W \propto L$ and $k=0.5$. Here we use M 7 as an

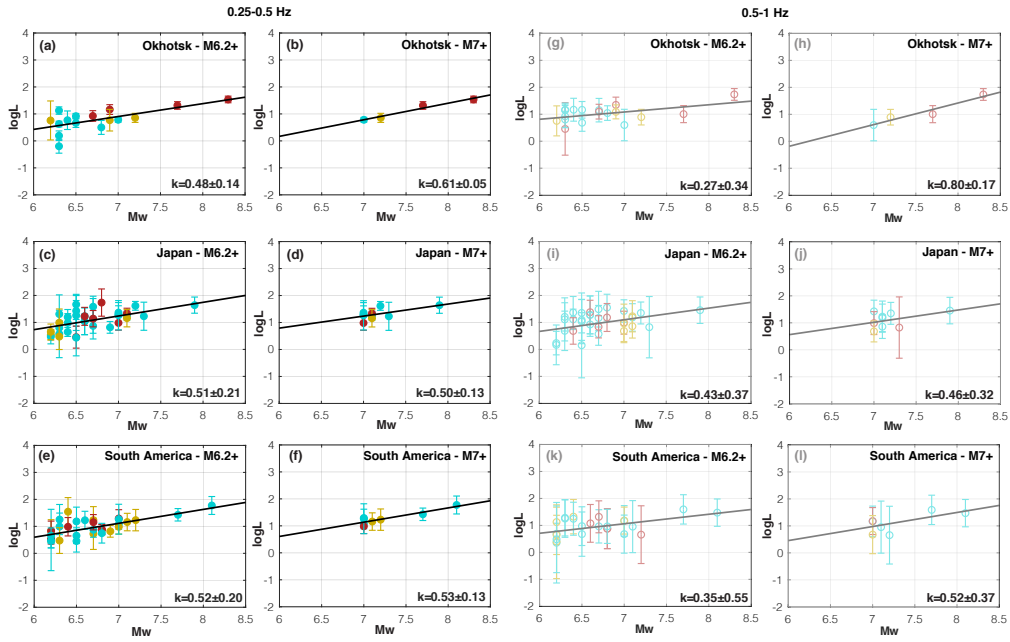


Figure 5. Moment-size scaling relation inferred from the array coherence decay rate of US-Array in the Eastern US. (a-f): in 0.25-0.5 Hz; (g-l): in 0.5-1 Hz. (a,b,g,k): the Sea of Okhotsk subduction zone; (c,d,i,j): Japan subduction zone; (e,f,k,l): South America subduction zone. (a,c,e,g,i,k): events with $M_w > 6.2$; (b,d,f,h,j,l): events with $M_w > 7$. The k-value (slope) of the fitted scaling relation curve k is indicated in each subfigure. Colors are coded for different focal depths: blue: shallow earthquakes (< 70 km), orange: intermediate earthquakes ($70 - 300$ km), red: deep-focus earthquakes (> 300 km). The uncertainty of each earthquake is estimated by error propagation theory.

empirical transition magnitude between quasi-equal-dimensional and elongated ruptures (Scholz, 2019).

Previous scaling relation studies based on finite-fault inversions, geodetic and geological surveys manifest consistent k-value as theoretical models (Blaser et al., 2010; Leonard, 2010; Goda et al., 2016; Gomberg et al., 2016; Allen & Hayes, 2017; S et al., 2017; Brengman et al., 2019) (dots in Figure 6). Most of the measurements of M4 to M6 class earthquakes show k-values around 0.5 (Blaser et al., 2010; Leonard, 2010; Goda et al., 2016; Gomberg et al., 2016; S et al., 2017; Brengman et al., 2019), suggesting quasi-equal-dimensional rupture. For M7 class earthquakes, Gomberg et al. (2016) reported $k=0.78$, which is close to the L-model. However, Allen & Hayes (2017) reported a $k=0.63$, which is in between the quasi-equal-dimensional rupture model and the L-model.

The k-values estimated by array-coherence decay measurements in the three subduction zones show good consistency with those studies (squares and stars in Figure 6). For M7+ earthquakes, the k-value of the Sea of Okhotsk (0.61) are in-between the quasi-equal-dimensional model and L-model, which are compatible with the measurement of other subduction interface earthquakes by Allen & Hayes (2017). The k-values of the Japan and South American subduction zones are around 0.5 (0.53 and 0.50), which is close to the quasi-equal-dimensional model. The consistency of scaling relation derived from array coherence decay indicates that the array coherence decay is a good proxy of rupture size of large earthquakes ($M_w > 7$). For M6 class earthquakes, the k-values of all the three subduction zones are around 0.5, which are close to the quasi-equal-dimensional model. The earthquake depth distribution seems not affect the scaling relation too much, while the magnitude distribution determines the uncertainty of scaling relation (k-value). It is clear that M 6.2 to M 7 earthquakes are highly scattered with large uncertainty in the coherence-measured rupture size. Therefore, the scaling relation (k-value) is more accurately estimated for M 7+ earthquakes. Since the rupture size estimation for M 6-7 earthquakes have large uncertainties, the k-value near 0.5 can only indicate that the coherence roughly constrains the order-of-magnitude of the rupture size.

We argue that M7+ earthquakes are in the transition of two scaling relations of small-magnitude (M6 class, quasi-equal-dimensional) and large-magnitude (M7+, $L \gg W$) earthquakes reported by Gomberg et al. (2016); Luo et al. (2017), which is between 0.5 and 0.75. The transition magnitude is related to the seismogenic width W (Luo et al.,

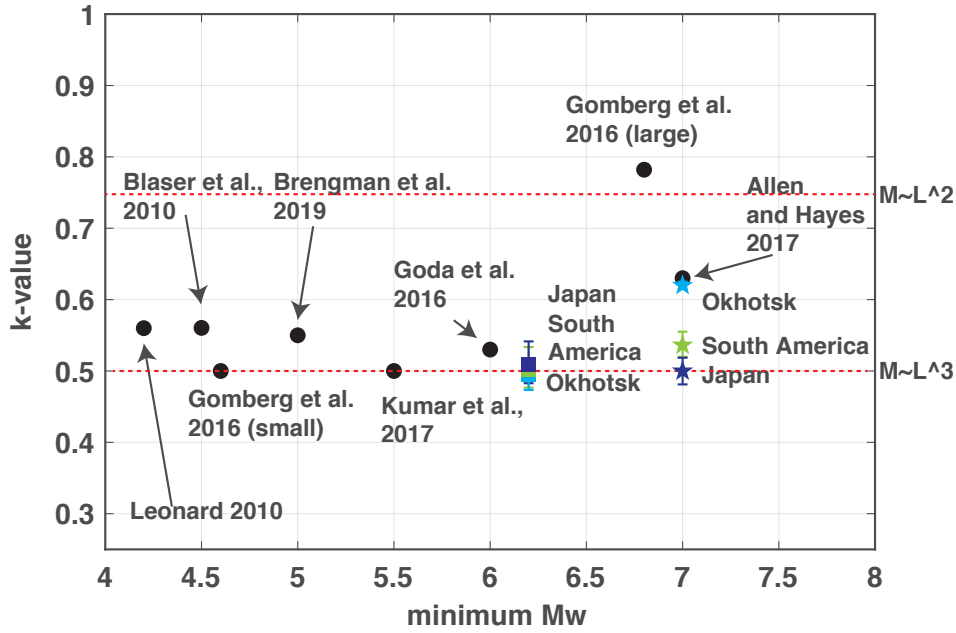


Figure 6. Comparison of the coherence-inferred k-values in different regions and k-values inferred from other scaling relation studies. Black dots: k-values and minimum moment magnitudes of previous scaling relation studies. Squares: coherence-inferred k-value for M6 class earthquakes. Stars: coherence-inferred k-value for M7+ earthquakes. Squares and stars are color coded by subduction zones. The uncertainty of each earthquake is estimated by error propagation theory.

2017), which contributes to the variation of k-values. Different distributions of seismogenic width controlled by variations of slab geometry and along-dip rheology may also be responsible for regional variation of k-values in different subduction zones. Furthermore, the variations of the k-value in different subduction zones may be indicators of scale-dependence of rigidity or stress drop (Izutani & Kanamori, 2001), which is related to spatial heterogeneities of the rupture region (Cocco et al., 2016). If the scaling of rigidity or stress drop with rupture size is expressed by $\mu(\Delta\sigma) \propto L^\alpha$ (Geller, 1976), then the k-value can be expressed by $k = 1.5/(n + \alpha)$. The k-value for earthquakes with scale-dependent rigidity or stress drop is smaller than the k-value for earthquakes with scale-invariant fault parameters.

The variation of k-value between different subduction zones may indicate different transition magnitudes and different scale-dependent source parameters. These properties are further affected by the seismogenic width, geometry/rheological properties along the fault plane, and velocity weakening/strengthening properties related to temperature or subduction materials. For example, the Sea of Okhotsk subduction zone earthquakes show larger k-value which may indicate that the seismogenic width is easily to be saturated. The complex relation between k-value variations and subduction zone properties requires further studies.

5 Discussion

Here, we analyze the uncertainties of the coherence-based rupture size estimation method in different aspects, including finite frequency, earthquake source complexities including aspect ratio of earthquake rupture, bilateral rupture, etc. We also give our prospective of this unique coherence-based earthquake rupture size estimation method and the possible future applications.

5.1 Finite-frequency effects

Note that equation (6) is valid for monochromatic waves, therefore it applies to array recordings filtered in a narrow frequency band. The complete form of the coherence equation requires a weighted integral of equation (3) over the frequency range of interest, which does not have an analytical form. We compute the array coherence of the elongated rupture model for various source sizes using the narrow-band integration (equa-

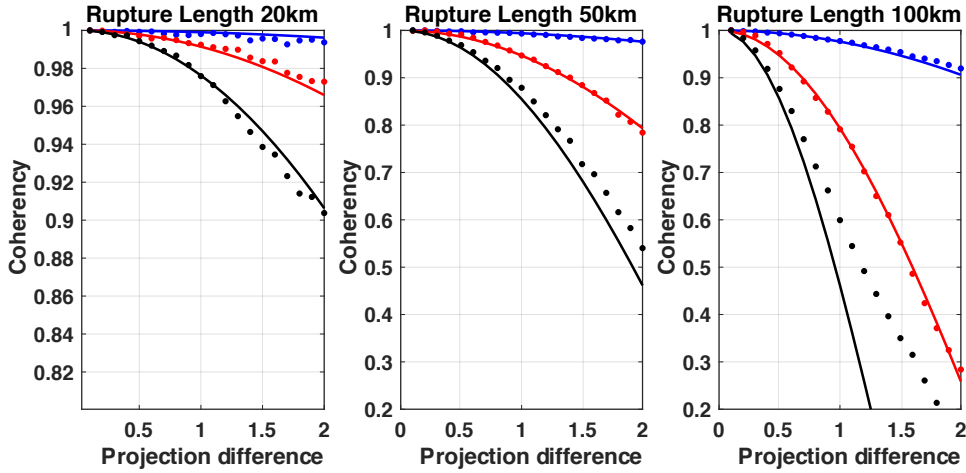


Figure 7. Simulated coherence decay as a function of inter-station projection difference. The array is located at 30 degrees from the source. The rupture velocity is assumed to be 3 km/s. We consider three rupture lengths, 20, 50, and 100 km. The coherence pattern is shown in three frequency ranges: 0.25-0.5 Hz (blue), 0.5-1 Hz (red), and 1-2 Hz (black). Dots: coherence computed using narrow-band frequency integration (equation 3); Solid lines: coherence computed using theoretical monochromatic simulation (equation 6) in the median frequency (0.375 (blue), 0.75 (red) and 1.5 Hz (black)).

tion 3) in three frequency bands (0.25-0.5, 0.5-1 and 1-2 Hz) and theoretical monochromatic simulation (equation 6) in the median frequency of the three frequency bands (i.e., 0.375, 0.75 and 1.5 Hz) (Figure 7). The resulting coherence pattern shows the features anticipated from the estimation of the Sea of Okhotsk earthquakes: it decreases monotonically as a function of projection difference; it decays faster at higher frequencies; and for a given frequency range, a larger rupture length results in faster coherence decay. Besides, the two lower frequency bands (0.5-0.25 and 0.5-1 Hz, also the two selected frequency ranges for further analysis) manifest consistent coherence pattern between numerical narrow-band integration and theoretical monochromatic simulation. The coherence pattern for projection differences up to 2 degrees is almost identical, especially for large rupture lengths (> 100 km) (Figure 7). There are notable difference between the monochromatic simulation and narrow-band integration in 1-2 Hz for the rupture length of 100 km due to finite frequency effects.

5.2 Effects of Source Complexity on Rupture Size Estimation

Since we apply a unilateral 1D rupture model to fit the array coherence decay function, deviation from this rupture model may induce uncertainties in the rupture size estimation. Kinematic rupture properties, such as different aspect ratio (L/W), bilateral vs unilateral rupture propagation, and variation of rupture speeds, are expected to introduce additional complexities.

Rupture Speed

Rupture speed is eliminated in monochromatic equation (6), however the complete form of integrating equation (3) over the frequency range will introduce second-order terms involving the rupture speed. We conduct a synthetic test to demonstrate the effect of the rupture speed in our selected narrow frequency bands (Figure 8). The rupture length is assumed to be 100 km. In the frequency bands of 0.25-0.5 and 0.5-1 Hz, the effect of rupture speed is minor since the coherence decay pattern is nearly identical for rupture speed of 2.5, 3, 3.5 and 4 km/s (Figure 8). The maximum deviation of the CC value at projection difference of 1 degree is only 0.0019 and 0.027 for 0.25-0.5 Hz and 0.5-1 Hz, respectively, which correlates to the rupture length deviation of 0.1 km and 1.6 km, respectively. The nearly identical coherence pattern ensures little uncertainty in the estimation of rupture size in the two narrow frequency ranges.

Rupture Aspect Ratios

The rupture aspect ratio also influences the uncertainty of rupture length estimates from array coherence decay rates. Since we assume $L \gg W$, the main rupture direction is along the strike and the waveform coherence is only influenced by a series of 1D rupture patches (equation 5). 2D rupture effects are not negligible when considering a rupture with lower aspect ratio. In such cases, the rupture direction is not along the strike and the teleseismic waveform consists of multiple components from 2D fault patches. The coherence pattern is therefore more complex and does not have an explicit form. Here, we further consider a 2-D rupture model to analyze the effects of rupture aspect ratio L/W on the array coherence approach. The teleseismic wavefield of a 2-D Haskell's source model is

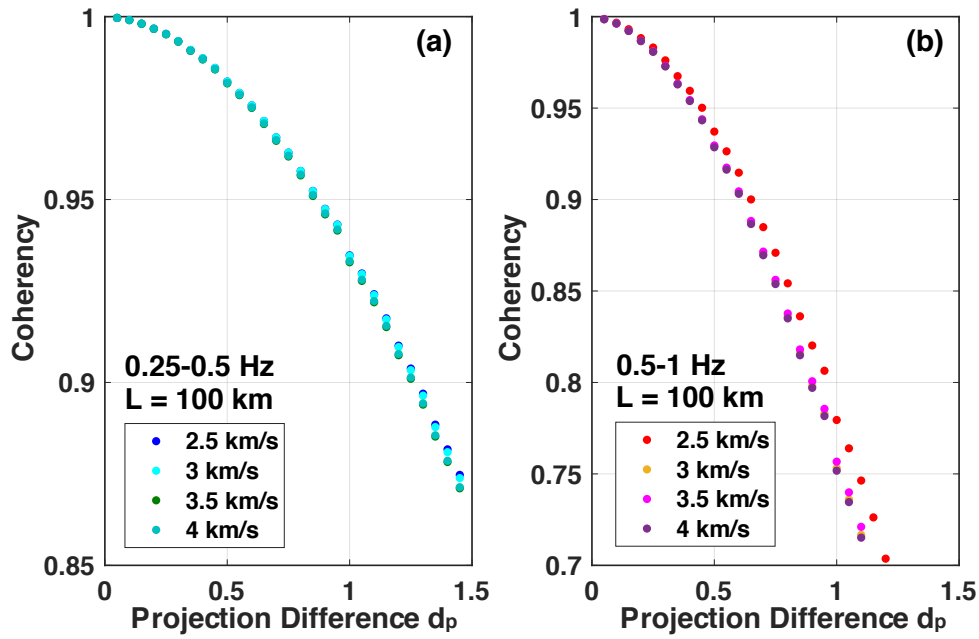


Figure 8. Simulated coherence pattern for an elongated Haskell's source model with different rupture speeds (2.5, 3, 3.5 and 4.5 km/s). Coherence is presented as a function of projection difference d_p . Rupture length is assumed to be 100 km. Station and fault settings are the same as Figure 7. (a) coherence pattern in 0.25-0.5 Hz; (b) coherence pattern in 0.5-1 Hz.

$$u(r, \phi, t) = \frac{\mu}{4\pi\rho c^3} \int_0^L \int_0^W \frac{R}{r} \dot{D}\left(t - \frac{r}{c} - \frac{x}{V_{rx}} - \frac{y}{V_{ry}} + \frac{\sqrt{x^2 + y^2} \cos \phi \sin \theta}{c}\right) dx dy, \quad (10)$$

429 where $1/V_{rx}$ and $1/V_{ry}$ are the components of the rupture slowness vector along the
 430 x (rupture length L) and y (rupture width W) directions, respectively. The seismic record-
 431 ing at a station is now a surface integral along the rupture area. Equation 10 does not
 432 have analytical solutions for a general case, so we conduct numerical simulations to demon-
 433 strate the effects of rupture complexity. To simplify the simulation, we assume the rup-
 434 ture width W is constant, such that $L \gg W$. Under this assumption we integrate equa-
 435 tion 10 and get the far-field monochromatic wavefield as:

$$u(\omega, T) = \frac{\mu RW}{4\pi\rho c^3 r} \dot{D}(\omega) e^{-\frac{i\omega r}{c}} (H_Z e^{-iZ} + H_Y e^{-iY}) \quad (11)$$

436 where $Z = \omega L/2 * (1/V_{rx} - \sin \theta \cos \phi/c)$, and $Y = \omega L/2 * (1/V_{ry} + \sin \theta \cos \phi/c)$.
 437 $H(Z)$ and $H(Y)$ are the sinc functions of Z and Y , respectively.

438 We conduct a synthetic test using different rupture lengths and different aspect ra-
 439 tios in 0.25 - 0.5 Hz (Figure 9) to test the valid L/W range in which our assumption of
 440 elongated rupture applies. We find larger ruptures generally allow a lower valid L/W ra-
 441 tio than smaller ruptures. If we consider 20% uncertainty of the rupture length is accept-
 442 able, L/W needs to be greater than 5 for $L = 50$ km, but can be as low as 2.5 for $L =$
 443 100 km. The lower threshold of valid L/W ratio for larger events may explain why the
 444 array coherence decay rate estimation is more suitable for large earthquakes ($M_w > 7$).

445 **Bilateral Ruptures**

446 A bilateral rupture case is also a deviation from the unilateral rupture assumed in
 447 equation 5. To simplify the analysis, we consider a symmetric bilateral rupture with rup-
 448 ture length L , which can be regarded as the sum of two unilateral ruptures of length $L/2$
 449 propagating in opposite directions simultaneously. Theoretically, the relation between
 450 coherence and projection difference is

$$\text{acos}(\text{CC}) = \frac{\omega L d_p}{4c} + \delta, \quad (12)$$

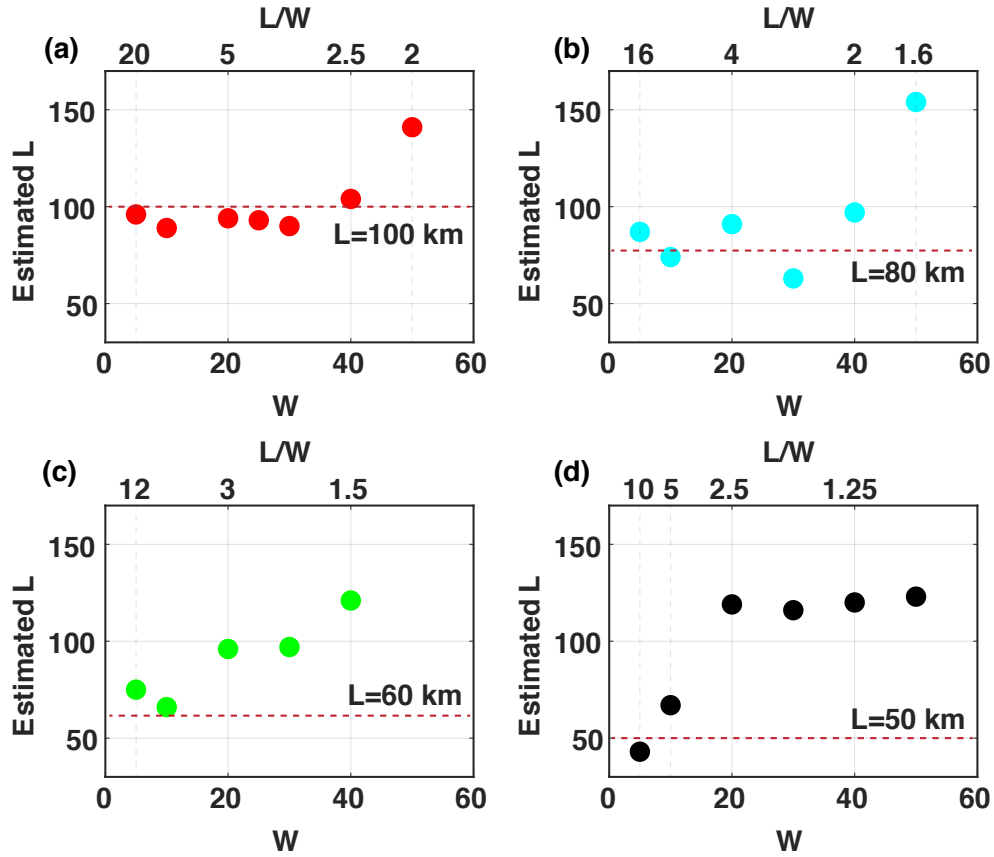


Figure 9. The effect of aspect ratio (L/W) on coherence estimated rupture size in 0.25-0.5 Hz frequency band. (a-d) are tested with true rupture length of 100, 80, 60 and 50 km, respectively. The rupture velocity is assumed to be 3 km/s. Coherence estimated rupture length is plotted as a function of rupture width W (bottom axis) and corresponding aspect ratio L/W (top axis). Red dashed lines indicate the true rupture length.

451 The denominator of the first term on the right-hand side in equation (12) is $4c$, in-
452 stead of $2c$ in equation (8). Thus a symmetric 1D bilateral rupture reduces the inter-station
453 coherence decay rate by $1/2$. Therefore, for a symmetric bilateral rupture, the estimated
454 length assuming a unilateral rupture is half the true length. An example is the 2013 M
455 8.3 Sea of Okhotsk earthquake. Based on back-projection and finite-fault inversions, (Meng
456 et al., 2014; Ye et al., 2013; Wei et al., 2013), this earthquake has two rupture branches
457 propagating northeastward and southwestward, respectively. The coherence-based rup-
458 ture length estimation is 49 km. If considering the bilateral rupture correction, the es-
459 timated rupture length will be 98 km, which is closer and within one order of magnitude
460 of the back-projection estimated rupture length of 145 km. There's still underestima-
461 tion of the rupture size, partially because this earthquake has a complex rupture pro-
462 cess with multiple rupture branches.

463 More realistic bilateral rupture model can be described with a 2D rupture. Here
464 we conduct a synthetic test of a $W * L = 10 * 50$ km rupture dimension for both the
465 unilateral and bilateral ruptures using equation (11) (Figure 10(a-d)). The pattern of
466 coherence decay with projection difference deviates from the cosine-shaped function for
467 projection difference larger than 0.5 and the coherence decay is faster compared to 1D
468 rupture model. Bilateral rupture is also observed to reduce the coherence decay rate. For
469 example, with a rupture speed of 2.5 km/s, the coherence estimated rupture length in
470 the 0.25-0.5 Hz frequency band is 56 km for a unilateral rupture and 35 km for the bi-
471 lateral rupture. Rupture size estimation using a 1D source model for bilateral rupture
472 will lead to a rupture size underestimation of 30%. Theoretically, one could estimate the
473 rupture size using a bilateral rupture model or a 2D rupture model with inversion meth-
474 ods. However, bilateral ruptures in reality are hardly symmetric, which can not be ex-
475 pressed in an explicit form for estimating the rupture length directly. Moreover, inter-
476 ference between the two rupture fronts create extra waveform complexities which adds
477 much uncertainty to the array coherence measurement. Therefore in this paper, while
478 we analyze and discuss the effects of bilateral ruptures, we still apply an elongated uni-
479 lateral rupture model to examine the rupture lengths.

480 The coherence measured rupture size may be more representative of the main as-
481 perity than the entire rupture. Large earthquakes usually show slip heterogeneities (Brown
482 et al., 2015), where multiple areas of large slip are separated by small slip patches, act-
483 ing as asperities or sub-sources. Since the assumption of our coherence method is based

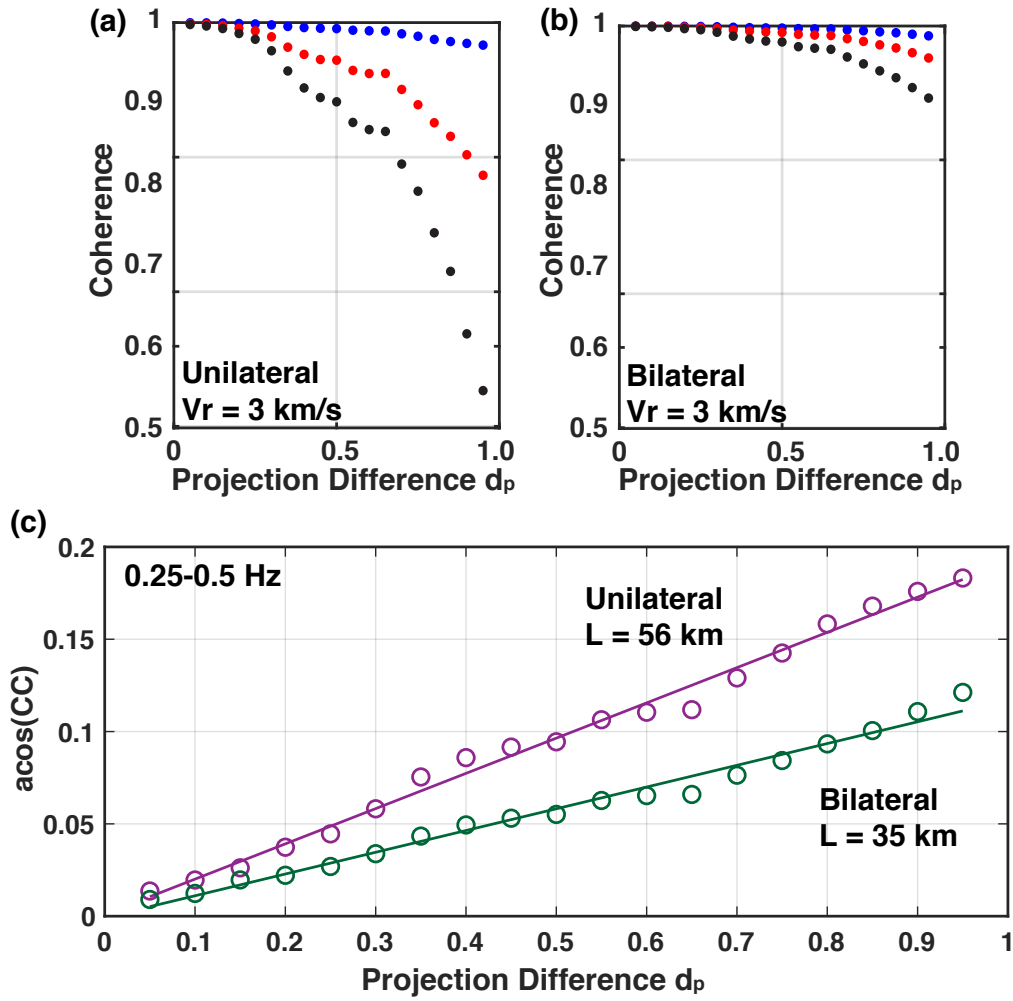


Figure 10. Coherence decay curve as a function of projection difference d_p for 2-D unilateral and bilateral ruptures and the corresponding rupture length estimates. (a) unilateral rupture; (b) bilateral rupture. Three frequency bands are color coded with blue (0.25-0.5 Hz), red (0.5-1 Hz) and black (1-2 Hz). The rupture dimension is set as 10 km along dip and 50 km along strike. The rupture speed is set as 3 km/s. Synthetic coherence are computed using equation 11. (c) rupture size estimation in 0.25-0.5 Hz for coherence decay curves (a) and (b). Unilateral rupture and bilateral rupture are color coded by purple and dark green, respectively. The rupture length estimation is using 1D model (equation 8.)

484 on waveforms generating from a continuous rupture area, the main asperity of a large
485 earthquake may take control of the waveform coherence. Therefore, the underestimation
486 of the rupture size of certain large earthquakes (e.g., the M 8.3 Sea of Okhotsk) may be
487 caused by slip heterogeneity.

488 **5.3 Future Work of Coherence Based Source Analysis**

489 We observe a salient feature that the array coherence decay rate depends on earth-
490 quake source size. A simple analytical relation, under the assumption of an elongated
491 Haskell's source model, is able to explain that the coherence behavior is generally gov-
492 erned by the earthquake source size. We further develop a method to measure source size
493 from the coherence curve, assuming a simple unilateral rupture model. The method can
494 give an approximate estimation for fault rupture sizes for the main asperity. For deep
495 and oceanic earthquakes, where satellite geodesy is unavailable, source dimension is con-
496 ventionally inferred from finite-fault source inversion or back-projection. Teleseismic-only
497 finite-fault inversions generally suffer from non-uniqueness due to trade-off between source
498 size and rupture speed. Back-projection can generally map the trajectory of the rupture,
499 but coda waves and scatterings can generate uncertainties in determining when the earth-
500 quake stops, which adds uncertainty to the rupture size. Hence, estimated source sizes
501 are subject to large variabilities. We can utilize the coherence curve as an alternative
502 to cross-validate the inferred source size. If the estimated size is close to the true size
503 , the synthetic coherence curve should match the observation. The observation of the
504 relation between array coherence decay rate and earthquake rupture size also potentially
505 provides additional constraints to discriminate physical models of subduction zone earth-
506 quakes derived from numerical simulations and laboratory experiments.

507 **6 Conclusion**

508 In this study, we report a new observation of the relation between earthquake rup-
509 ture size and the decay rate of inter-station waveform coherence as a function of projec-
510 tion difference within an seismic array. We observe that coherence is predominantly mod-
511 ulated by source size for large earthquakes ($M_w > 7$) in the frequencies above the earth-
512 quake's corner frequency; it decays faster if the source size is larger. Increasing the source
513 size causes a larger inter-station difference of phase delays between seismic waves from
514 different parts of the source, resulting in a breakdown of waveform coherence. Assum-

515 ing a simple elongated Haskell's source model, the array coherence decay can be used
 516 to roughly estimate the rupture size L . The inferred rupture size satisfies empirical scal-
 517 ing relations between rupture length and moment magnitude. Furthermore, our estima-
 518 tion shows that the scaling exponent between rupture length and magnitude of large earth-
 519 quakes ($M_w > 7$) is in between 0.5 to 0.75 for several subduction zones, which corre-
 520 sponds to the transition from the quasi-equal-dimensional source model and the L-model.
 521 Despite the uncertainties coming from rupture aspect ratio, bilateral rupture, and struc-
 522 tural heterogeneities, our proposed method has the potential to cross-validate source sizes
 523 from other studies and to fill the gap of rupture size estimation for deep and remote earth-
 524 quakes.

525 Appendix A Derivation of equation 7

526 We start from the definition of the cross-correlation coefficient in the frequency do-
 527 main:

$$CC(\omega) = \frac{\text{Real}(U(S_A, \omega) \cdot U^*(S_B, \omega))}{|U(S_A, \omega)| \cdot |U(S_B, \omega)|}. \quad (\text{A1})$$

528 Substituting equation (5), the numerator of CC is:

$$\text{NUM} = \text{Real}(U(S_A, \omega) \cdot U^*(S_B, \omega)) = C_{AB} \exp \left[-i\omega \left(\frac{r_A - r_B}{c} + \frac{L(S_A - S_B)}{2} + g_A - g_B \right) \right], \quad (\text{A2})$$

529 where

$$C_{AB} = \frac{\mu^2 R^2 W^2 G_A G_B}{16\pi^2 \rho^2 c^6 r_A r_B} \dot{D}^2(\omega) \frac{1}{\omega^2 S_A S_B} \sin \left(\frac{\omega L}{2} S_A \right) \sin \left(\frac{\omega L}{2} S_B \right). \quad (\text{A3})$$

530 Using the Euler's formula and taking the real part, we get

$$\text{NUM} = C_{AB} \cos \left[\omega \left(\frac{r_A - r_B}{c} + \frac{L(S_A - S_B)}{2} + g_A - g_B \right) \right]. \quad (\text{A4})$$

531 Substituting equation 5 in the denominator of CC, we get:

$$\text{DEN} = |U(S_A, \omega)| \cdot |U(S_B, \omega)| = C_{AB} \sqrt{\left| \exp \left[-i\omega \left(\frac{r_A}{c} + \frac{LS_A}{2} + g_A \right) \right] \right|^2} \cdot \sqrt{\left| \exp \left[-i\omega \left(\frac{r_B}{c} + \frac{LS_B}{2} + g_B \right) \right] \right|^2}. \quad (\text{A5})$$

532 Given that

$$|\exp(-i\theta)|^2 = (\cos \theta)^2 + (-\sin \theta)^2 = 1, \quad (\text{A6})$$

equation (A5) is reduced to:

$$\text{DEN} = C_{AB} \cdot \sqrt{1} \cdot \sqrt{1} = C_{AB}. \quad (\text{A7})$$

533 Next, dividing the numerator (equation A4) by the denominator (equation A7),

534 we get

$$\text{CC} = \cos \left[\omega \left(\frac{r_A - r_B}{c} + \frac{L(S_A - S_B)}{2} + g_A - g_B \right) \right]. \quad (\text{A8})$$

535 Here, the first term $(r_A - r_B)/c$ is the travel time difference from the epicenter to
 536 the two different stations A and B. Since we aligned the waveform by the first P arrival,
 537 this term can be eliminated. The CC value only depends on the second and third terms
 538 which are related to the source size $(L(S_A - S_B)/2)$ and the difference between local path
 539 and site effects $(g_A - g_B)$. Substituting the definition of the slowness term $S = 1/V_r -$
 540 γ/c (equation 4), we get

$$\text{CC} = \cos \left[\frac{\omega L}{2c} (\gamma_A - \gamma_B) + \omega (g_A - g_B) \right] \quad (\text{A9})$$

541 which is equation 6.

542 Acknowledgments

543 This research was supported by NSF EAR1848486 and by Leon and Joann V.C. Knopoff
 544 Fund. Our broadband earthquake data set is obtained from FDSN (<https://www.fdsn.org>)
 545 downloaded by ObsPy (<https://github.com/obspy/obspy/wiki>). The networks used are
 546 TA (IRIS Transportable Array. (2003). USArray Transportable Array. International Fed-
 547 eration of Digital Seismograph Networks. <https://doi.org/10.7914/SN/TA>), IU (Albu-
 548 querque Seismological Laboratory (ASL)/USGS. (1988). Global Seismograph Network

549 (GSN - IRIS/USGS). International Federation of Digital Seismograph Networks. <https://doi.org/10.7914/SN/IU>),
 550 II (Scripps Institution Of Oceanography. (1986). IRIS/IDA Seismic Network. Interna-
 551 tional Federation of Digital Seismograph Networks. <https://doi.org/10.7914/SN/II>), US
 552 (Albuquerque Seismological Laboratory (ASL)/USGS. (1990). United States National
 553 Seismic Network. International Federation of Digital Seismograph Networks. <https://doi.org/10.7914/SN/US>),
 554 and AK (Alaska Earthquake Center, U. O. A. F. (1987). Alaska Regional Network. In-
 555 ternational Federation of Digital Seismograph Networks. <https://doi.org/10.7914/SN/AK>).
 556 We are grateful to the Global Centroid Moment Tensor Catalog (<https://www.globalcmt.org/>)
 557 for the earthquake catalog with moment tensor solutions.

558 References

- 559 Aki, K., & Richards, P. G. (2002). *Quantitative seismology*.
- 560 Allen, T. I., & Hayes, G. P. (2017). Alternative rupture-scaling relationships for
 561 subduction interface and other offshore environments. *Bulletin of the Seismological*
 562 *Society of America*, 107(3), 1240–1253.
- 563 Bevington, P. R., & Robinson, D. K. (2002). *Data reduction and error analysis for*
 564 *the physical sciences (3rd ed.)*. McGraw-Hill.
- 565 Blaser, L., Krüger, F., Ohrnberger, M., & Scherbaum, F. (2010). Scaling relations of
 566 earthquake source parameter estimates with special focus on subduction environ-
 567 ment. *Bulletin of the Seismological Society of America*, 100(6), 2914–2926.
- 568 Brengman, C. M., Barnhart, W. D., Mankin, E. H., & Miller, C. N. (2019).
 569 Earthquake-scaling relationships from geodetically derived slip distributions.
 570 *Bulletin of the Seismological Society of America*, 109(5), 1701–1715.
- 571 Brown, L., Wang, K., & Sun, T. (2015). Static stress drop in the mw 9 tohoku-
 572 oki earthquake: Heterogeneous distribution and low average value. *Geophysical*
 573 *Research Letters*, 42(24), 10–595.
- 574 Burdick, S., Vernon, F. L., Martynov, V., Eakins, J., Cox, T., Tyttell, J., . . . oth-
 575 ers (2017). Model update may 2016: Upper-mantle heterogeneity beneath north
 576 america from travel-time tomography with global and usarray data. *Seismological*
 577 *Research Letters*, 88(2A), 319–325.
- 578 Chen, Y., Wen, L., & Ji, C. (2014). A cascading failure during the 24 may 2013
 579 great okhotsk deep earthquake. *Journal of Geophysical Research: Solid Earth*,
 580 119(4), 3035–3049.

- 581 Cocco, M., Tinti, E., & Cirella, A. (2016). On the scale dependence of earthquake
582 stress drop. *Journal of Seismology*, *20*(4), 1151–1170.
- 583 Efron, B., & Tibshirani, R. J. (1994). *An introduction to the bootstrap*. CRC press.
- 584 Ekström, G., Nettles, M., & Dziewoński, A. (2012). The global cmt project 2004–
585 2010: Centroid-moment tensors for 13,017 earthquakes. *Physics of the Earth and*
586 *Planetary Interiors*, *200*, 1–9.
- 587 Geller, R. J. (1976). Scaling relations for earthquake source parameters and magni-
588 tudes. *Bulletin of the Seismological Society of America*, *66*(5), 1501–1523.
- 589 Gibbons, S. J., & Ringdal, F. (2006). The detection of low magnitude seismic
590 events using array-based waveform correlation. *Geophysical Journal International*,
591 *165*(1), 149–166.
- 592 Goda, K., Yasuda, T., Mori, N., & Maruyama, T. (2016). New scaling relationships
593 of earthquake source parameters for stochastic tsunami simulation. *Coastal Engi-
594 neering Journal*, *58*(3), 1650010–1.
- 595 Gomberg, J., Wech, A., Creager, K., Obara, K., & Agnew, D. (2016). Reconsidering
596 earthquake scaling. *Geophysical Research Letters*, *43*(12), 6243–6251.
- 597 Haskell, N. (1964). Total energy and energy spectral density of elastic wave ra-
598 diation from propagating faults. *Bulletin of the Seismological Society of America*,
599 *54*(6A), 1811–1841.
- 600 Hawthorne, J., & Ampuero, J.-P. (2018). A phase coherence approach to identify-
601 ing co-located earthquakes and tremor. *Geophysical Journal International*, *209*(2),
602 623–642.
- 603 Hawthorne, J., Thomas, A., & Ampuero, J.-P. (2019). The rupture extent of low fre-
604 quency earthquakes near parkfield, ca. *Geophysical Journal International*, *216*(1),
605 621–639.
- 606 Ide, S. (2007). Dynamic rupture propagation on a 2d fault with fractal frictional
607 properties. *Earth, planets and space*, *59*(10), 1099–1109.
- 608 Izutani, Y., & Kanamori, H. (2001). Scale-dependence of seismic energy-to-moment
609 ratio for strike-slip earthquakes in japan. *Geophysical research letters*, *28*(20),
610 4007–4010.
- 611 Ji, C., Wald, D. J., & Helmberger, D. V. (2002). Source description of the 1999
612 hector mine, california, earthquake, part i: Wavelet domain inversion theory and
613 resolution analysis. *Bulletin of the Seismological Society of America*, *92*(4), 1192–

614 1207.

615 Kiser, E., & Ishii, M. (2017). Back-projection imaging of earthquakes. *Annual Re-*
616 *view of Earth and Planetary Sciences*, *45*, 271–299.

617 Langston, C. A. (2014). Coherence of teleseismic p and s waves across the trans-
618 portable array. *Bulletin of the Seismological Society of America*, *104*(5), 2253–
619 2265.

620 Leonard, M. (2010). Earthquake fault scaling: Self-consistent relating of rupture
621 length, width, average displacement, and moment release. *Bulletin of the Seismo-*
622 *logical Society of America*, *100*(5A), 1971–1988.

623 Lin, F.-C., Li, D., Clayton, R. W., & Hollis, D. (2013). High-resolution 3d shallow
624 crustal structure in long beach, california: Application of ambient noise tomogra-
625 phy on a dense seismic array. *Geophysics*, *78*(4), Q45–Q56.

626 Luo, Y., Ampuero, J.-P., Miyakoshi, K., & Irikura, K. (2017). Surface rupture effects
627 on earthquake moment-area scaling relations. *Pure and Applied Geophysics*, *174*,
628 3331–3342.

629 Meng, L., Ampuero, J.-P., & Bürgmann, R. (2014). The 2013 okhotsk deep-focus
630 earthquake: Rupture beyond the metastable olivine wedge and thermally con-
631 trolled rise time near the edge of a slab. *Geophysical Research Letters*, *41*(11),
632 3779–3785.

633 Meng, L., Bao, H., Huang, H., Zhang, A., Bloore, A., & Liu, Z. (2018). Double
634 pincer movement: encircling rupture splitting during the 2015 mw 8.3 illapel
635 earthquake. *Earth and Planetary Science Letters*, *495*, 164–173.

636 Mordret, A., Brenguier, F., Causse, M., Boué, P., Voisin, C., Dumont, I., ... Am-
637 puero, J.-P. (2020). Seismic stereometry reveals preparatory behavior and source
638 kinematics of intermediate-size earthquakes. *Geophysical research letters*, *47*(17),
639 e2020GL088563.

640 Obara, K. (2012). New detection of tremor triggered in hokkaido, northern japan by
641 the 2004 sumatra–andaman earthquake. *Geophysical research letters*, *39*(20).

642 Park, S., & Ishii, M. (2015). Inversion for rupture properties based upon 3-d direc-
643 tivity effect and application to deep earthquakes in the sea of okhotsk region. *Geo-*
644 *physical Journal International*, *203*(2), 1011–1025.

645 Peng, Z., & Zhao, P. (2009). Migration of early aftershocks following the 2004 park-
646 field earthquake. *Nature Geoscience*, *2*(12), 877–881.

- 647 Poli, P., Thomas, C., Campillo, M., & Pedersen, H. A. (2015). Imaging the d'' reflec-
648 tor with noise correlations. *Geophysical Research Letters*, *42*(1), 60–65.
- 649 Riahi, N., & Gerstoft, P. (2015). The seismic traffic footprint: Tracking trains, air-
650 craft, and cars seismically. *Geophysical Research Letters*, *42*(8), 2674–2681.
- 651 Romanowicz, B., & Rundle, J. B. (1993). On scaling relations for large earthquakes.
652 *Bulletin of the Seismological Society of America*, *83*(4), 1294–1297.
- 653 S, T. K. K., Martin Mai, P., & Goda, K. (2017). New empirical earthquake source-
654 scaling laws. *Bulletin of the Seismological Society of America*, *107*(5), 2225–2246.
- 655 Scholz, C. H. (2019). *The mechanics of earthquakes and faulting*. Cambridge univer-
656 sity press.
- 657 Shelly, D. R., Beroza, G. C., & Ide, S. (2007). Non-volcanic tremor and low-
658 frequency earthquake swarms. *Nature*, *446*(7133), 305–307.
- 659 Shen, W., & Ritzwoller, M. H. (2016). Crustal and uppermost mantle structure
660 beneath the united states. *Journal of Geophysical Research: Solid Earth*, *121*(6),
661 4306–4342.
- 662 Wei, S., Helmberger, D., Zhan, Z., & Graves, R. (2013). Rupture complexity of
663 the mw 8.3 sea of okhotsk earthquake: Rapid triggering of complementary earth-
664 quakes? *Geophysical Research Letters*, *40*(19), 5034–5039.
- 665 Ye, L., Lay, T., Kanamori, H., & Koper, K. D. (2013). Energy release of the 2013
666 mw 8.3 sea of okhotsk earthquake and deep slab stress heterogeneity. *Science*,
667 *341*(6152), 1380–1384.
- 668 Zerva, A., & Zervas, V. (2002). Spatial variation of seismic ground motions: an
669 overview. *Appl. Mech. Rev.*, *55*(3), 271–297.
- 670 Zhan, Z., Kanamori, H., Tsai, V. C., Helmberger, D. V., & Wei, S. (2014). Rupture
671 complexity of the 1994 bolivia and 2013 sea of okhotsk deep earthquakes. *Earth
672 and Planetary Science Letters*, *385*, 89–96.